SUPPLEMENTARY MATERIAL

S1 PFT classes and the corresponding isoprene basal emission factors in MEGANv2

		PLANT FUNCTIONAL TYPES	EMISSION FACTORS in µg $m^{-2}h^{-1}$
TREES	1.	Needleleaf Evergreen, Temperate	600
	2.	Needleleaf Evergreen, Boreal	3,000
	3.	Needleleaf Deciduous, Boreal	1
	4.	Broadleaf Evergreen, Tropical	7,000
	5.	Broadleaf Evergreen, Temperate	10,000
	6.	Broadleaf Deciduous, Tropical	7,000
	7.	Broadleaf Deciduous, Temperate	10,000
	8.	Broadleaf Deciduous, Boreal	11,000
SHRUBS	9.	Broadleaf Evergreen, Temperate	2,000
	10.	Broadleaf Deciduous, Temperate	4,000
	11.	Broadleaf Deciduous, Boreal	4,000
GRASS	12.	C3 Arctic Grass	1,600
	13.	C3 non-Arctic Grass	800
	14.	C4 Grass	200
CROP	15.	Crop	1

Table S1: The 16 plant functional types compatible with the Community Land Model (CLM) used in MEGANv2.

S2 Diagram of consecutive transformations applied on LULC datasets

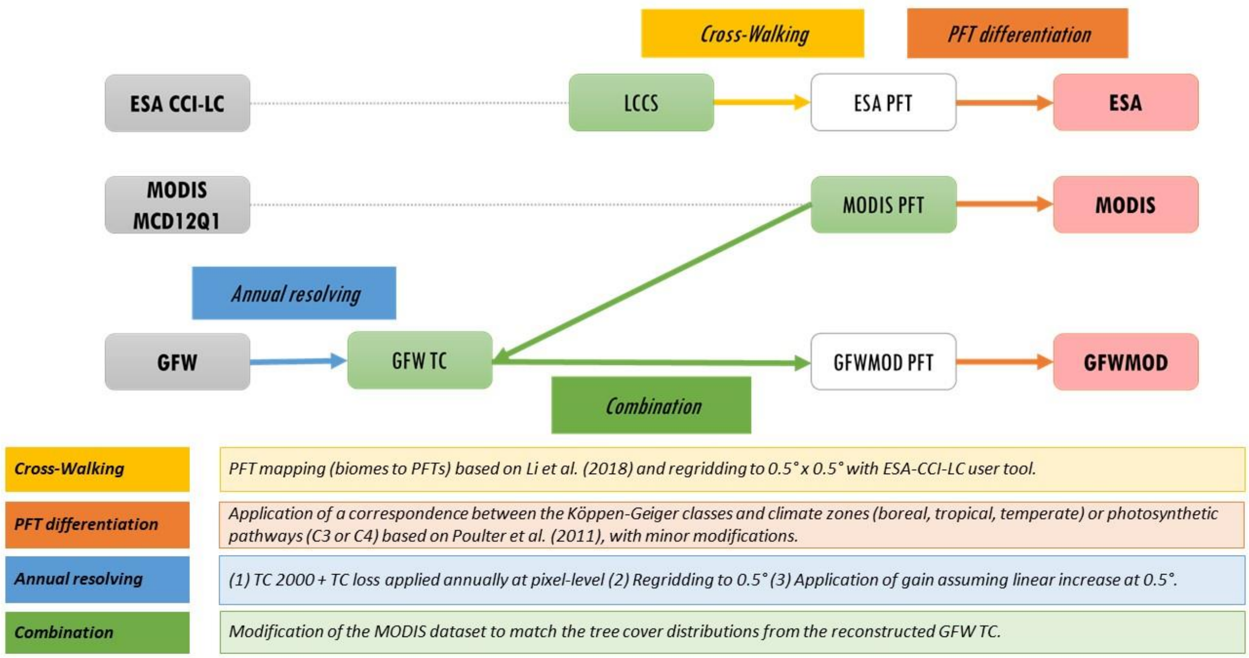

Figure S1: Schematic representation of the consecutive transformations applied on the original datasets (in grey boxes) to generate annually updated LULC maps comprising 16 PFTs, compatible with the MEGAN model (in red boxes). Initial (annually resolved) and intermediate maps are in green and white boxes, respectively. Transformations are represented by arrows with a short description inset.

S3 Distributions of the climate zones and C3/C4 photosynthetic pathways

The differentiation into climate zones and photosynthetic pathways applied on trees, shrubs and grasses was performed based on Table 3 from Poulter et al. (2011). A few adjustments were applied on their Table 3. The updated Köppen-Geiger classes are listed in Table S2. Classes 'Dfa' and 'Dfb' were reclassified as temperate instead of boreal types because the boreal ecoregion was protruding southward over Eastern Europe and North-East USA, below the established transition latitude at about 50° N (Hall et al., 2004). Besides, certain C3 (classified as 'cool' in Table 3) and C4 ('warm' in Table 3) classes have been interchanged ('BWk', 'BSk', 'Csa', 'Dwa', 'Dfb') for a better agreement with the literature on the topic (Woodward et al., 2004; Shoko et al., 2016) and the CLM map, for which the mapping method of Still was applied using MODIS LAI (Still et al., 2003; Lawrence and Chase, 2007). In reality, certain regions are prone to the co-existence of C3 and C4 grasses species, but no mixed grassland is accounted for in this study. The original and modified distributions of biomes are shown in Figure S1.

	ORIGINAL	**MODIFIED**
TROPICAL	---	---
TEMPERATE		Dfa, Dfb
BOREAL	Dfa, Dfb	
WARM C4	BWk, BSk, Csa, Dwa	
COOL C3		BWk, BSk, Csa, Dfb
ARCTIC C3	Dfb	Dwa

Table S2: Correspondence between Köppen-Geiger classes and biomes/photosynthetic pathways that were reclassified for the present study. The original classification as in Table 3 of Poulter et al. (2011) is given in the second column; and the modified classification is given in the third column.

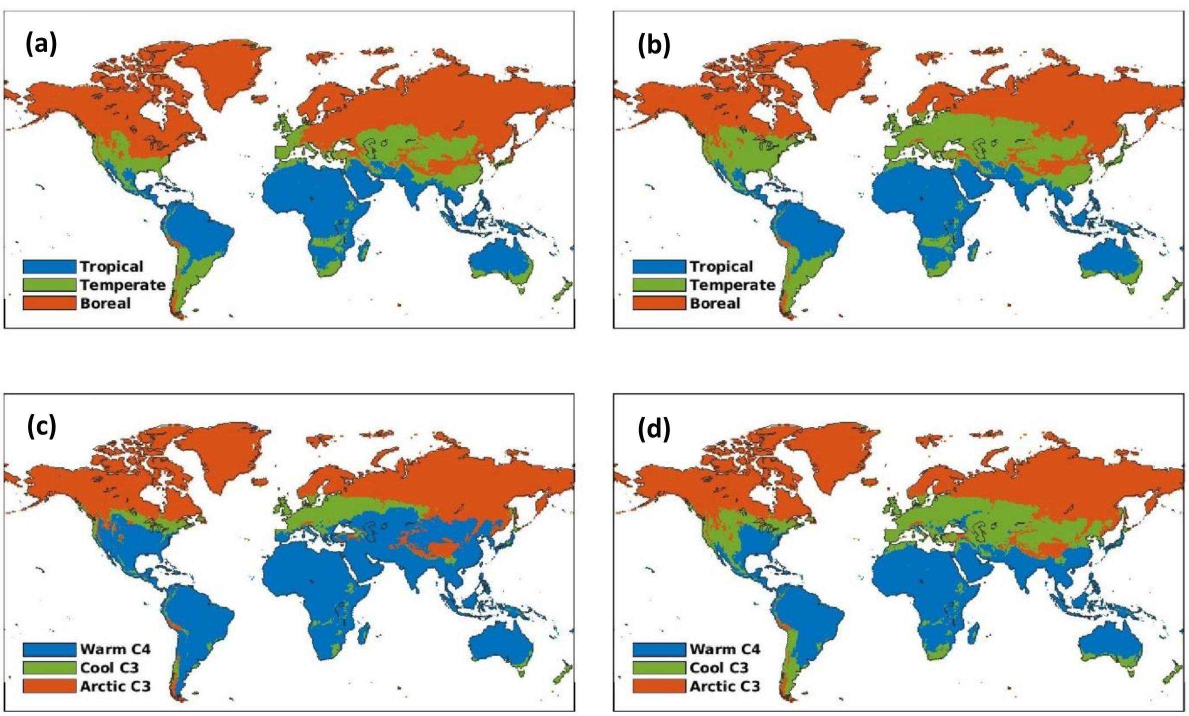

Figure S2: Differentiation according to climate zones (a: original, b: modified) and C3/C4 photosynthetic pathways (c: original, d: modified).

S4 Tree cover trends at global and regional scales (2001-2016)

UNITS: $km^2\ yr^{-1}$	MODIS	ESA	GFWMOD	FAOSTAT
TROPICAL	-14.6	-8.4	-51	---
BOREAL	15.1	-1.8	-21.5	---
TEMPERATE	18.4	1.3	-11.6	---
WORLD	18.2	-14	-83.5	-49.7

Table S3: Zonal and global tree cover trends (in $x10^3\ km^2\ yr^{-1}$) for the 2001-2016 period. The climate domains (tropical, temperate and boreal) were defined in Section 2.2.1. and shown in Figure S1.

UNITS: $km^2\ yr^{-1}$	US	BRAZIL	CHINA	INDONESIA	RUSSIA
FAOSTAT	4.4	-32.2	22.3	-3.9	4
MODIS	-2.2	-10.6	8.8	-0.8	9.3
ESA	-0.9	-0.9	-0.3	-2.5	0.03
GFWMOD	-6.6	-16.9	-2.5	-7.3	-7.7

Table S4: Net total trends (in x $10^3\ km^2\ yr^{-1}$) for the 2001-2016 of countries with large forested areas as provided by FAOSTAT, MODIS, ESA and GFWMOD.

S5 Differences in TC and global annual isoprene emissions in 2001

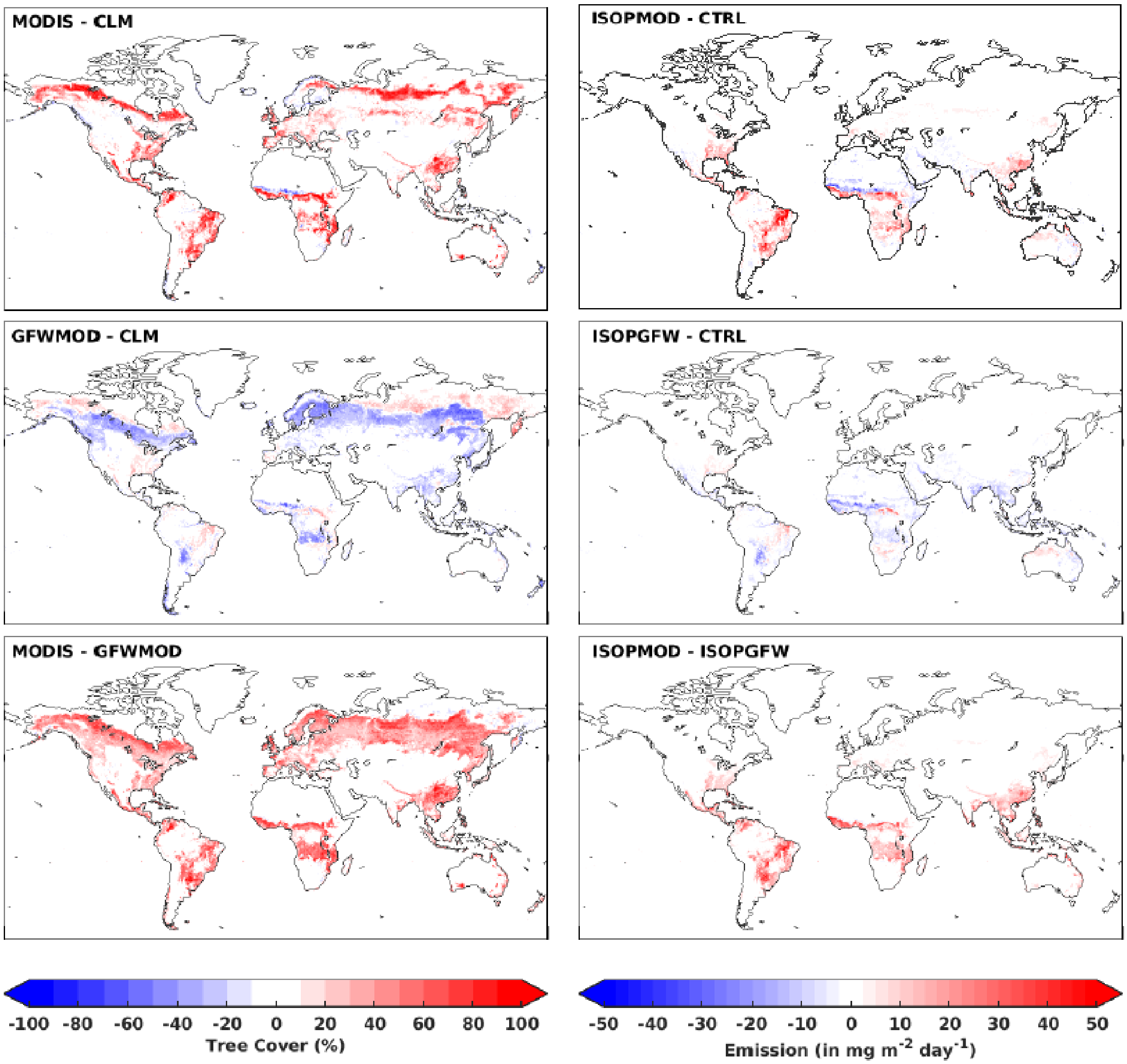

Figure S3: Differences in tree cover between the three datasets (left panel: MODIS – CLM, GFWMOD – CLM, and MODIS-GFWMOD), and corresponding differences between the annually-averaged isoprene emissions (right panel: ISOPMOD – CTRL, ISOPGFW – CTRL, and ISOPMOD – ISOPGFW).

S6 Effects of soil moisture stress and CO_2 inhibition on global emissions and trends

		Annual mean (in Tg)			Annual trends (in $\%yr^{-1}$)		
		CTRL	**ISOPMOD**	**ISOPGFW**	**CTRL**	**ISOPMOD**	**ISOPGFW**
Standard setup	$\gamma_{SM} = 1$ $\gamma_{CO_2} = 1$	418	520	354	0.94	0.90	0.61
SM effect	$G12$	363	464	314	1.00	0.92	0.61
CO_2 effect	$PW11$	404	502	342	0.36	0.35	0.08
SM and CO_2 effects	$G12$ $PW11$	369	471	320	0.79	0.72	0.42

Table S5: Global mean annual isoprene emissions (in Tg) and trends (in % yr^{-1}) for the 2001-2016 period in CTRL, ISOPMOD and ISOPGFW simulations. The first row shows estimations from the study run, whereas second to fourth rows show the impact of the soil moisture stress from Guenther et al. (2012) (G12) and/or the CO_2 inhibition following the parameterization of Possell and Hewitt (2011) (PW11).

The CO_2 inhibition effect is calculated based on the mean value of annual mean concentrations measured at Mauna Loa and South Pole stations. The formulation of Possell and Hewitt (2011) for the inhibition effect leads to a small decrease of global mean isoprene emissions by 3% but the offsetting effect on trends is substantial (-0.5 $\%yr^{-1}$). The use of the formulation of Heald et al. (2009) would lead to an increase of global emissions by about 1.5%, with a smaller cutback on the trend compared to the aforementioned formulation (-0.2 $\%yr^{-1}$). The soil moisture stress defined in Guenther et al. (2012) with $\Delta\theta_1 = 0.06$ has little effect on trends. The reduction of the global mean emissions is of the order of 10%, i.e. half of the reduction reported in the previous study of Müller et al. (2008) using MEGAN-MOHYCAN. This difference stems from the spatial differences in isoprene emissions resulting from the use of the gridded emission maps instead of using PFT maps with PFT-dependent emissions factors, as in the present study, and because of different versions of MODIS LAI products (Guenther et al., 2006; Jiang et al., 2017).

S7 Meteorological trends from ERA Interim

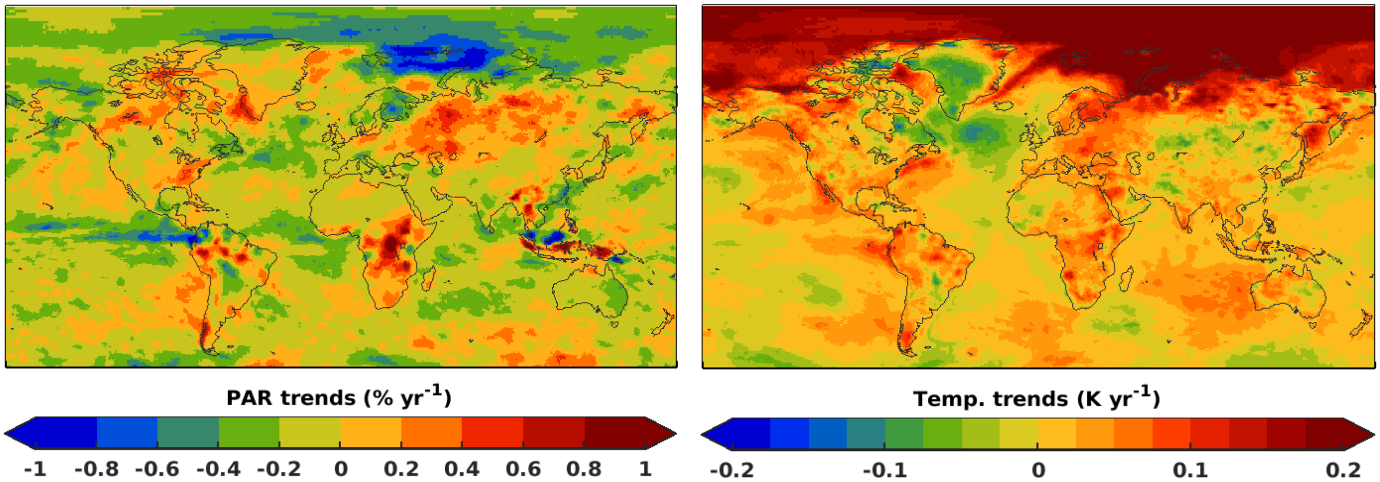

Figure S4: Distribution of trends of photosynthetically active radiation (PAR, in % yr^{-1}) and temperature (in K yr^{-1}) for the 2001-2016 period.

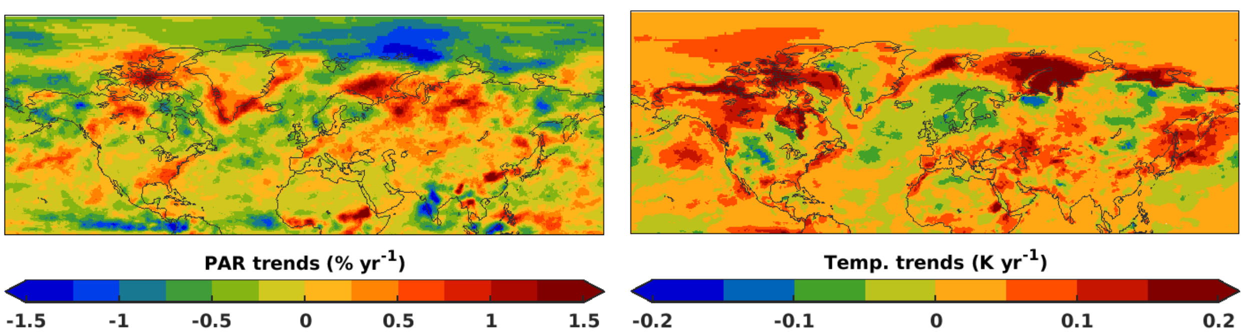

Figure S5: Distribution in trends of July-August means over the Northern Hemisphere. Despite the known Arctic-Amplification, the boreal summer trends of temperature and PAR conditions show a decreasing trends over 2001-2016 and is responsible of negative trends in isoprene emissions seen in Figure 7 over Siberia.

S8 Burnt biomass VOC

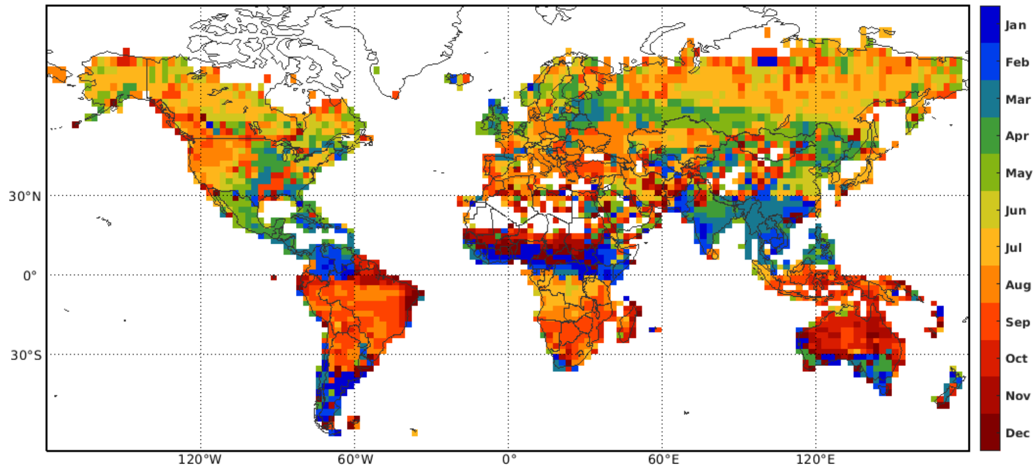

Figure S6: Middle month of the three-consecutive-month period with highest VOC emissions due to vegetation fires, based on climatological means of the GFED4s dataset for 2005-2016 (van der Werf et al., 2017) and emission factors of Andreae (2019).

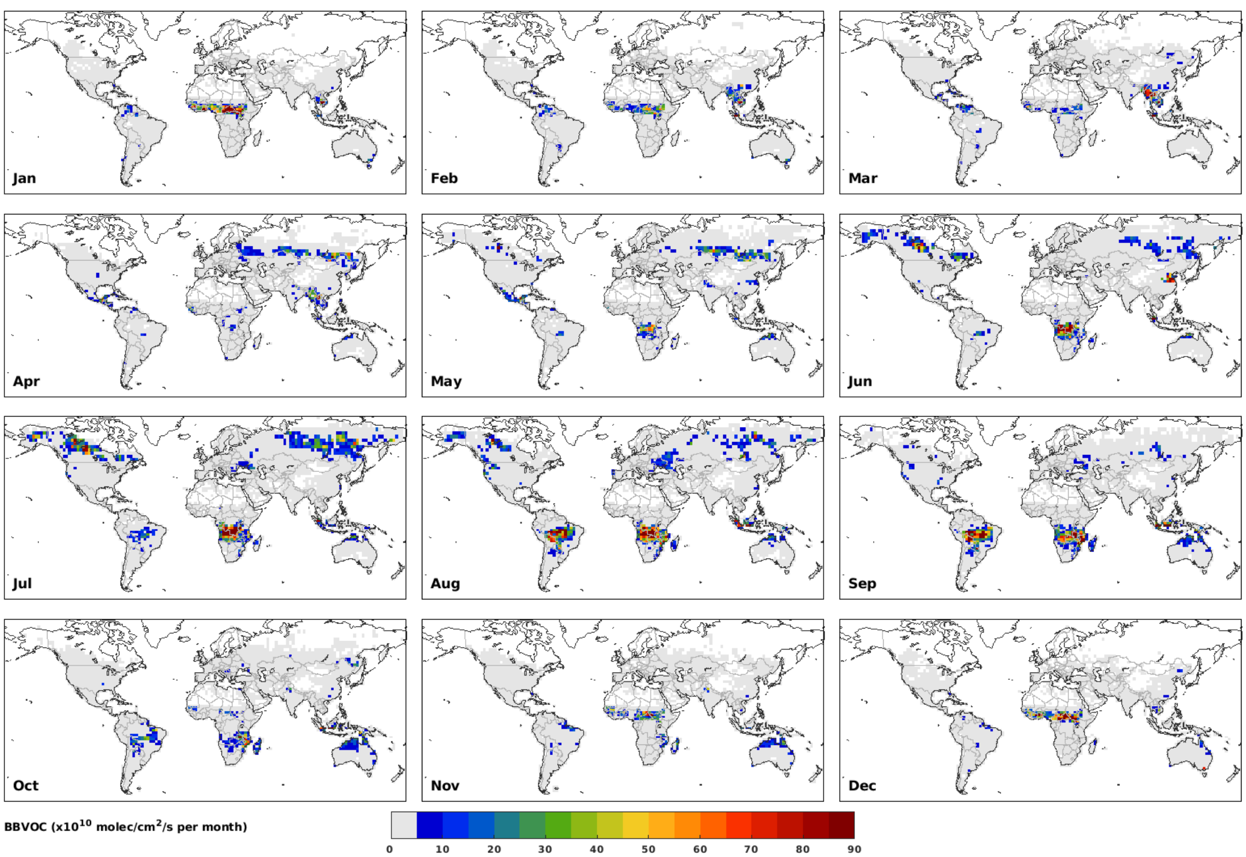

Figure S7: Monthly averaged distribution of biomass burning VOC emissions (in 10^{10} molec. cm^{-2} s^{-1}) based on a climatology of GFED4s flux data over 2005-2016 (van der Werf et al., 2017) and emission factors of Andreae (2019).

S9 Interannual variability

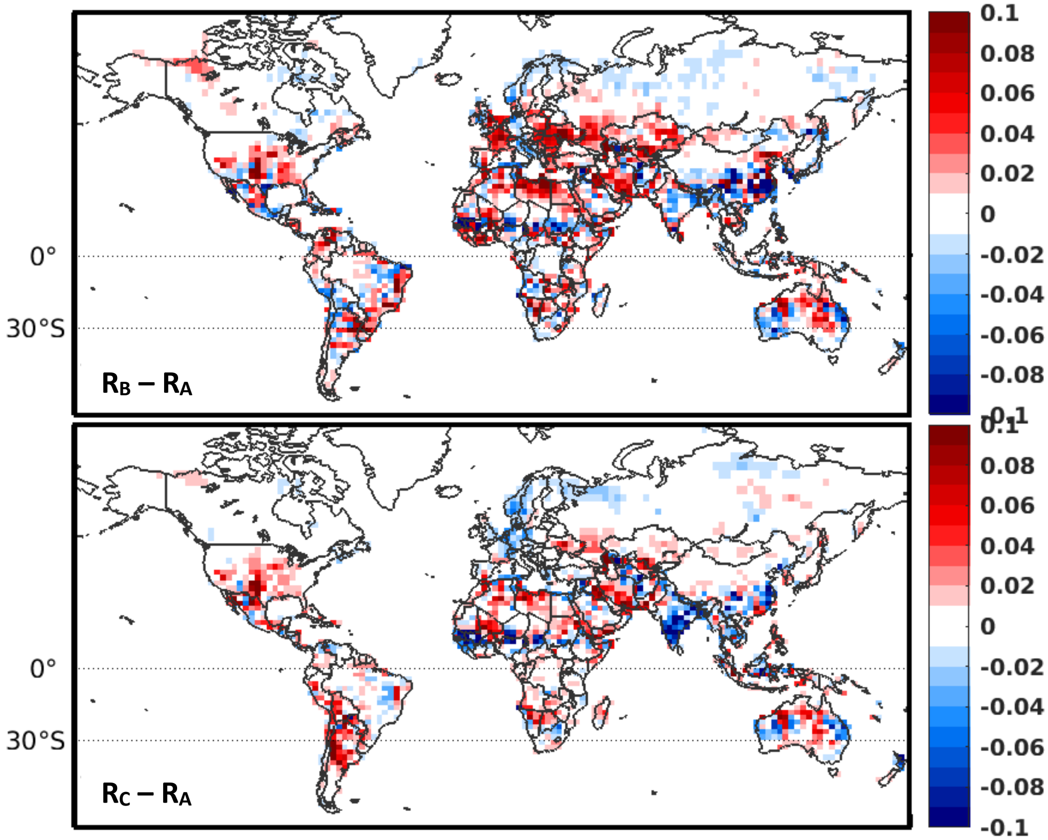

Figure S8: Upper panel: difference $R_B – R_A$ between the correlations coefficients of simulated HCHO columns from run B (R_B) and A (R_A) with OMI HCHO columns. Lower panel: difference $R_C – R_A$ between correlation coefficients of simulated columns from run C (R_C) and A (R_A) with OMI columns.

S10 Selected regions for evaluation

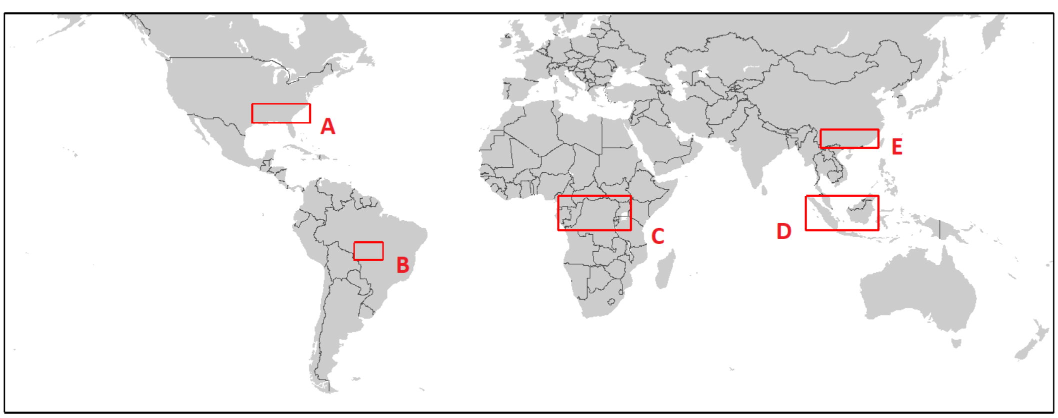

Figure S9: Map of selected regions for evaluation of HCHO interannual variability: (A) Southeastern US (30.1°-35.9° N, 77.6°-95° W), (B) Mato Grosso (10.1°-16° S, 50.1°-60°W), (C) Equatorial Africa (6°S-5.9° N, 10°-34.9° E), (D) Indonesia (5.9°S-5.9° N, 95°-119.9° E, and (E) South China (22°-27.9° N, 100°-119.9° E).

S11 Seasonal variability in Southeastern US and South China

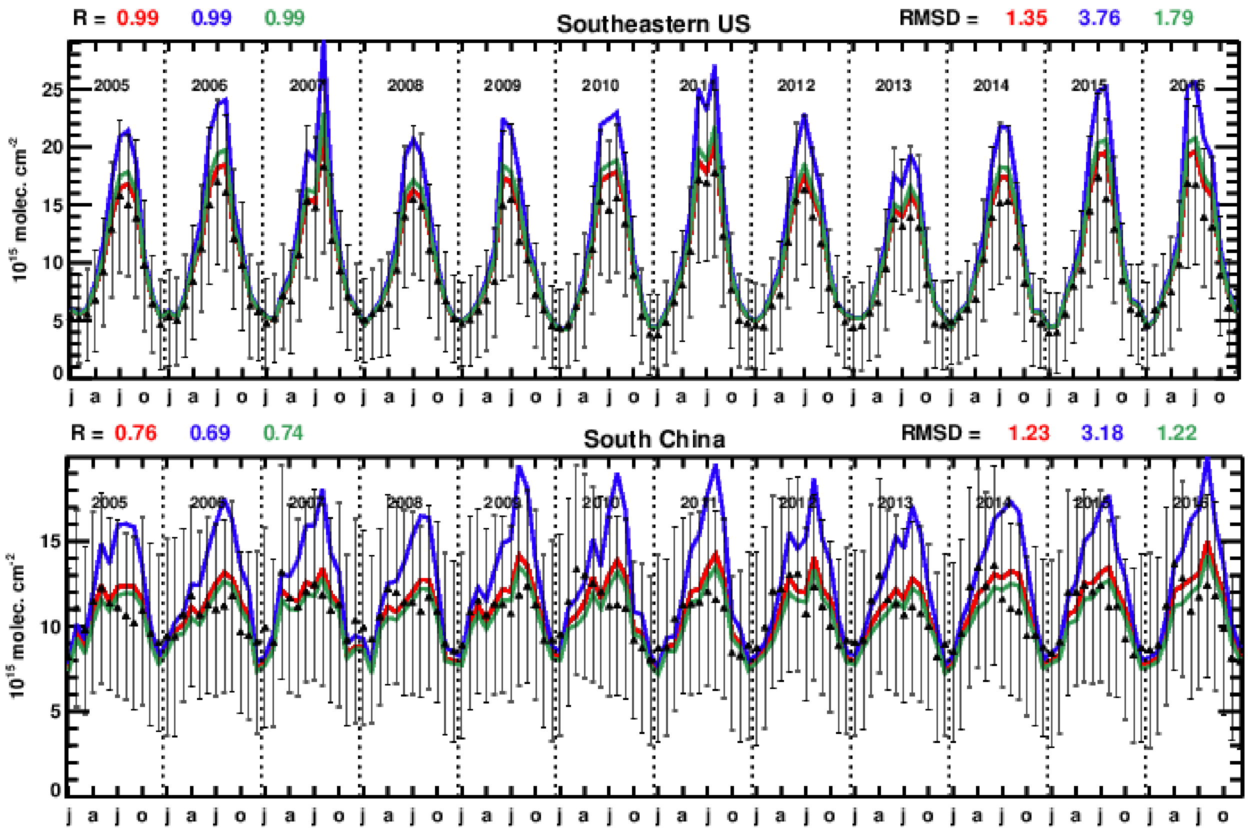

Figure S10: Time series over 2005-2016 of monthly averaged OMI HCHO columns (black triangles) and modelled HCHO over Southeastern US (upper panel) and South China (lower panel). The error bars represent the estimated OMI column uncertainties. The solid lines represent the model-calculated columns from runs A (red), B (blue) and C (green). The correlation coefficient (R) and the root-mean square deviations (RMSD) are given inset.